Hindawi
Journal of Sensors
Volume 2023, Article ID 9791652, 1 page
https://doi.org/10.1155/2023/9791652

Retraction

Retracted: Application of DC-DC Converter in Sensor and MEMS Device Integration and Packaging

Journal of Sensors

Received 19 December 2023; Accepted 19 December 2023; Published 20 December 2023

This article has been retracted by Hindawi following an investigation undertaken by the publisher [1]. This investigation has uncovered evidence of one or more of the following indicators of systematic manipulation of the publication process:

(1) Discrepancies in scope
(2) Discrepancies in the description of the research reported
(3) Discrepancies between the availability of data and the research described
(4) Inappropriate citations
(5) Incoherent, meaningless and/or irrelevant content included in the article
(6) Manipulated or compromised peer review

The presence of these indicators undermines our confidence in the integrity of the article's content and we cannot, therefore, vouch for its reliability. Please note that this notice is intended solely to alert readers that the content of this article is unreliable. We have not investigated whether authors were aware of or involved in the systematic manipulation of the publication process.

Wiley and Hindawi regrets that the usual quality checks did not identify these issues before publication and have since put additional measures in place to safeguard research integrity.

We wish to credit our own Research Integrity and Research Publishing teams and anonymous and named external researchers and research integrity experts for contributing to this investigation.

The corresponding author, as the representative of all authors, has been given the opportunity to register their agreement or disagreement to this retraction. We have kept a record of any response received.

References

[1] S. Wang, X. Ding, and Q. Tan, "Application of DC-DC Converter in Sensor and MEMS Device Integration and Packaging," *Journal of Sensors*, vol. 2022, Article ID 7834718, 11 pages, 2022.

Hindawi
Journal of Sensors
Volume 2022, Article ID 7834718, 11 pages
https://doi.org/10.1155/2022/7834718

Research Article

Application of DC-DC Converter in Sensor and MEMS Device Integration and Packaging

Shifeng Wang,[1] **Xueyong Ding**,[1] **and Qingji Tan**[2]

[1]*School of Science and Technology, University of Sanya, Sanya, Hainan 572099, China*
[2]*School of Mechanical Engineering, Heilongjiang Agricultural Reclamation Vocational College, Harbin, Heilongjiang 150025, China*

Correspondence should be addressed to Shifeng Wang; shifengwang@sanyau.edu.cn

Received 13 July 2022; Revised 27 August 2022; Accepted 5 September 2022; Published 22 September 2022

Academic Editor: Gengxin Sun

DC-DC (direct current controlled direct current) converter is the core control circuit in the field of power electronics technology. Based on the theory of sensors and MEMS (microelectromechanical systems), this paper constructs a DC-DC converter device integration and packaging model and proposes an enhanced current equalization technology with offset correction function suitable for two-phase DC-DC converters. Aiming at the generation mechanism of the output ripple of the two-phase DC-DC converter, the model adopts the ripple elimination technology based on the interleaved synchronous clock and the self-calibration interleaved time generator, so that each phase of the converter is accurately staggered within the full-load range, and the problem of output ripple amplitude is solved. During the simulation process, a high-performance two-phase DC-DC converter chip is designed and implemented, which includes an adaptive on-time control logic based on ripple feedback, a self-calibrating zero-current turn-off circuit, and a robust power switch transistor drive logic. The experimental results show that the full-load current of the chip reaches 6A, the peak efficiency is 91%, the phase-to-phase current error is <0.6%, and the output ripple is <9 mV. In the 90.265 V AC input, 0-10 W load range, the output voltage error is less than 0.96%, when the load is switched between no-load and full-load, and the system response speed is less than 200 ps, which effectively improves the overall performance of the DC-DC converter.

1. Introduction

Power electronic technology is widely used in various types of power converters, and the core of which is the control circuit of the power converter. With the continuous development of semiconductor technology, the power electronic control circuit has evolved from the original discrete component to the current integrated circuit, which constitutes an important type of semiconductor chip [1]. The classification of power management chips includes many subdivided fields. The researchers took the power supply of the central processing unit of the portable equipment as the entry point and analyzed the multiphase DC with different voltage input/output ranges. Several key technologies of DC converter chips are studied [2]. There is a body diode turn-on and turn-off process, the application of bidirectional DC-DC converters will introduce new losses [3–5], and the optimal design for the control and drive of this type of converter has not been able to obtain a better solution [6]; therefore, studying the optimal driving method of RC-IGBT (reverse conducting IGBT) bidirectional DC-DC converter can provide an effective solution to the problem of RC-IGBT body diode characteristics in the bidirectional DC-DC converter scenario, which is helpful for ensuring the reliability of this type of converter [7].

Switching power supplies are widely used in the DC power supply of electronic equipment, power equipment, and communication systems. In high-frequency switching power supplies, the DC-DC converter is the core [8]. With the development of semiconductor technology, large-scale integrated circuits with high integration and powerful functions continue to appear, which makes electronic equipment continue to shrink and reduce its weight. How to reduce the switching power supply is an important direction of switching power supply research [9–11], which requires the study of DC-DC converter topology, new materials, high-performance electronic components, etc. [12]. Electric

energy conversion technology, as a method of converting electric energy to other forms of energy [13], integrates power electronic equipment, actuators, and controls [14].

In view of the high-performance power supply and low standby power consumption of portable devices, this paper expands the number of DC-DC converter phases to four phases to improve the load capacity and proposes a special static power consumption optimization technology for the four-phase power consumption under extremely light load. The DC-DC converter provides a low-power operating mode and ensures smooth mode switching through hysteresis logic; at the same time, an improved high-precision current mirror sampling technology is proposed, combined with adaptive on-time control, "master-slave" current. The control circuit is negligible compared to the power stage losses. These losses vary in different situations. According to the actual application, the conditions of component selection and the rules of parameter design of general impedance converters are analyzed and explained in detail; and the circuit is simulated and verified; while achieving similar performance of similar studies, the converter consumes only 7 pA of quiescent current. Compared with traditional synchronous rectification, the adaptive synchronous rectification scheme proposed in this paper can achieve a maximum efficiency improvement of 3% under the condition of 20.60% load.

2. Related Work

In recent years, there have been new developments in various fields of power electronics. In terms of power electronic devices, power semiconductor devices can be divided into silicon-based semiconductors, gallium nitride semiconductors, and extremely wide band gap semiconductors. In terms of the design of DC converters, in addition to realizing the predetermined functions, to be practically applied to electronic equipment, certain conditions must be met [15], which is what we usually call performance requirements. The technical indicators of the voltage stabilizer can be generally divided into two types: one is the characteristic index including the allowable input voltage range, output voltage range, and output current, that is, the load capacity, etc., and the other is the quality index, that is, the performance parameter, the stability of the output voltage includes efficiency, output voltage load regulation, output voltage linear regulation, reference voltage regulation, and quiescent current [16].

Although the piecewise linear slope compensation method can reduce the influence of the slope compensation on the peak current, it cannot fundamentally solve the influence of the duty cycle change on the load capacity due to the limited amplitude. Aiming at the influence of slope compensation on peak current, Liu et al. [17] adopted the method of adjustable clamping voltage and successfully suppressed the influence of slope compensation effect on load capacity by designing a reed voltage that could change with the duty cycle. It has been verified by Ji and Liao [18] that it can be very effective to solve the influence of the duty cycle change on the load capacity after the introduction of slope compensation. In fact, this scheme can still be further optimized. Stauth [19] made the peak current completely independent of the ramp current and resistance by changing the structure of the reed voltage.

Relevant research shows that piecewise linear compensation is evolved on the basis of one linear compensation, and the duty cycle is divided into several intervals, each segment adopts a compensation slope, and the compensation slope of each interval is determined by its maximum duty cycle. In this way, not only the compensation slope of each segment meets the system stability requirements in the corresponding duty cycle range, but also the compensation current is greatly reduced. Jordan et al. [20] found that when the duty cycle is extremely large, once a 100% duty cycle occurs in a certain cycle, when the next cycle comes, because the switch tube continues to conduct, the sampling current always exists, and the superimposed level drops. If the ramp current is too small compared to the sampling current, the superimposed level bath will quickly reach the error voltage VC within a very short time at the beginning of the next cycle [21], and the switch will be turned off, making the cycle duty cycle smaller. Due to the long conduction time of the freewheel, the inductor current will drop sharply [22], which will lead to continuous conduction in subsequent cycles to maintain the output voltage stability. Once this happens, the loop will be disordered, and the output voltage ripple will become larger [23].

3. Modeling of DC-DC Converters in Sensor and MEMS Device Integration and Packaging

3.1. DC-DC Converter Architecture. In the DC-DC converter architecture, in order to obtain better voltage regulation accuracy and dynamic performance, a control circuit must be used to work with the main circuit. The control circuit includes an output sampling network, an error amplifier, a compensator, and a pulse-width modulator. When under heavy load, due to the large current, the conduction loss and switching loss of each component are in the majority proportion, and the relative proportion of the loss consumed by the control and peripheral circuits is very small. The commonly used methods are voltage-type $d(x,t)$ and current-type control $v(\text{in}) - v(\text{out})$. In order to make the simulation more accurate and the input impedance closer to the closed-loop situation, a double-loop method is adopted, which is connected by an inductor and a capacitor. During DC scanning $c(x,t) - s(x,t)$, the inductor is equivalent to a short circuit, and the capacitor can be regarded as an open circuit; while in AC analysis, the inductor $r(sourse)$ is equivalent to an open circuit, and the capacitor can be regarded as a short circuit.

$$1 - d(x,t) = \begin{cases} \max\ (\text{in}) - \max\ (\text{out}) \\ \partial v(\text{in}) - \partial v(\text{out}), \end{cases}$$
$$c(x,t) - s(x,t) = \frac{1 + sl/r(sourse)}{1 - sl/r(sourse)}. \quad (1)$$

When using circuit for experiments, the actual parameters

of the inductance are difficult to control, and it is also particularly vulnerable to various factors such as environment and frequency. To this end, the coil inductance in circuit is replaced by an active analog inductance based on the principle of a general impedance converter, so that the high precision of the inductance can be achieved and the control of the parameters of the entire circuit can be greatly improved. Among them, the PWM (pulse-width modulation) generator $v(x,p)$ is generally composed of a sawtooth wave generator and a comparator $y(x-p)$. The sawtooth wave generator emits a sawtooth wave with a fixed amplitude and a fixed repetition frequency.

$$y\left(\sqrt{1+4m(x)},b\right)/v(x,p) \geq 1-y(x-p),$$
$$\frac{v(\text{in})-v(ou)}{1-v(\text{in})-v(ou)} \geq \frac{D(\text{in})-D(\text{out})}{1-x\left(\sqrt{d-a}\right)}. \tag{2}$$

When the DC-DC converter works in IGBT (insulated gate bipolar translator) conduction mode $D(\text{in})-D(\text{out})$, the other power tube $I(v)$ that is not effectively controlled will be in the off state of both body IGBT and body diode; when working in diode freewheeling mode, it is not effective. At the same time, the parameter value $1-v$ of the inductance can be adjusted by adjusting the resistance or capacitance parameters of the inductance in the general impedance converter $c(o)$, so that the inductance can be adjusted in a large range, which is beneficial to the adjustment of circuit parameters. In addition, if the circuit $L(p,q)dpdq$ using the active analog inductor based on the principle of the general impedance converter is used as a unit circuit.

$$I(v,\text{in},\text{out}) = \frac{v(\text{in})-v(ou)}{1-v} - [D(\text{in})+D(\text{out})],$$
$$\frac{1-c(o)}{c(o)}\int L(equation,q)dpdt - L_{cls}(p,q)dpdq = 1. \tag{3}$$

Among the switching nonisolated step-down switching converters, represented by DC-DC converters, this circuit is a single-tube nonisolated DC converter whose output voltage without a transformer is equal to or less than the input voltage. Among them, the double hysteresis current direction detection method considers the adverse effects of output current harmonics and glitches on the current direction detection $R(x)C(x)$ and can reliably identify the RC-IGBT type bidirectional DC, and the control signal $r(1-x)$ is switched to the effectively controlled power tube $r(d)-r(cr)$; the voltage and current double closed-loop control is used to quickly and accurately adjust the amplitude of the output voltage $c(x)$.

$$R(x)C(x) = \frac{\sqrt{\Delta r(1-x)}-\Delta r(c(x)-1)}{r(d)-r(cr)},$$
$$I(v,t) = \begin{cases} \dfrac{v}{1-v}, dt(x) < t < t(x) \\ D(t)+D(dt). \end{cases} \tag{4}$$

In a bidirectional DC-DC converter $dt(x)$, the equivalent DC input voltage vs and the output voltage vo on the DC bus side change continuously during the switching cycle $D(t)$, the voltage changes within a switching cycle are small, and the state space variable switching can be used. The so-called hysteresis loss refers to the hysteresis phenomenon of magnetic materials, which is related to frequency, voltage, and the square of the maximum magnetic flux density; and eddy current loss refers to the magnetic circuit.

3.2. Classification of DC Converters. When driving the gate of the power switch tube, it is necessary to separate the ground potential of the internal DC converter control circuit from the power ground to prevent the crosstalk from causing great noise $i(sense)-i(res)$ to the internal control circuit when the power tube is performing fast switching operations. Therefore, after the duty cycle signal $t(sense)$ of the control circuit and the zero-current turn-off signal Vz undergo a series of logical processing $di(x,t)$, it is necessary to convert the ground $dc(x,t)$ to a level conversion circuit, and the signals generated by the conversion control the switches of the upper and lower power transistors $\max(d)$ and $\max(x)$, respectively.

$$v(i)-v(o) = (i(sense)-4i(res))\frac{v}{1-v} - t(sense)/t(x),$$
$$i(sense)-4i(res) = \begin{cases} \left.\dfrac{dc(x,t)}{di}\right|_{\min(d)-\min(x)} \\ \left.\dfrac{di(x,t)}{di}\right|_{\max(d)-\max(x)}. \end{cases} \tag{5}$$

In order to eliminate the influence of noise, after a short leading edge blanking time, the dynamic comparator (DCMP) is activated to detect the voltage difference between the SW point and the PGND (protect ground) point. Comparing the bode plots before and after compensation in the figure, the phase angle margin after compensation is larger, so the compensation stability $R(x)-C(x)$ of the rear system is enhanced.

$$2\frac{R(x)C(x)}{1-f(x)C(x)} = \frac{\sqrt{R(x)C(x)}-1}{R(x)-C(x)} - \frac{\sqrt{R(x)C(x)}+1}{R(x)+C(x)}.$$
$$sigma[d(y,x)] = \begin{cases} lap\{dy(k)/dk, dx(k)/dk\} \\ 0. \end{cases} \tag{6}$$

The resistor array $R(x)+C(x)$ is adjusted according to the decoder output $Q[15:0]$ adjustment, so that the input positive offset of $dy(k)/dk$ is reduced. Because if the cross-over frequency of the open-loop transfer function is too high, the high-frequency switching frequency and its harmonics and high-frequency components caused by parasitic oscillations cannot be effectively suppressed. The system cannot work stably. Moreover, the cross-over frequency

should be located on the line segment with a slope of -20 dB/dec. If the slope of the mid-band is -20 dB/dec, the system $r(ref) - r(x)$ must be stable.

$$\begin{cases} \dfrac{r(ref) - r(x)}{r(ref) + r(x)} - r < 1 \\ (1 - r)v^t v \longrightarrow 1, \end{cases} \tag{7}$$

$$\begin{cases} i(a) = I(a) + \overline{I(a) + i(a)} + \overline{I(a)} \\ i(b) = I(b) + \overline{I(b) + i(b)} + \overline{I(b)}. \end{cases}$$

Under light load conditions, the converter $r(ref) + r(x)$ works in the discontinuous mode $i(a)$ of the inductor current. When the magnetic flux changes, the induced eddy current is generated in the iron core. This phenomenon is related to the square of the frequency, the voltage, and the square of the maximum magnetic flux density.

This prevents reverse inductor current and improves light load efficiency $I(a)$. If there is reverse current, the voltage at point SW will be higher than the voltage of power ground PGND. It is worth noting that turning off the lower power tube $I(b)$ too early when the inductor energy is not exhausted will cause transient oscillation of the output; turning off the lower power tube too late when the reverse inductor current has occurred will reduce the system efficiency.

The output voltage of the circuit proposed in Figure 1 can be adjusted by PWM, and the output voltage characteristic is also similar to the traditional DC-DC converter with L-C filtering. And because this circuit is a first-order system, there is no overshoot problem in the transient process. According to the structure of the RC-IGBT bidirectional DC-DC converter mentioned above, the simulation model of the bidirectional DC-DC converter working in the DC-DC and Boost modes is built in the PSIM 9.0.3 simulation environment, and the voltage and current dual modes are analyzed. In actual power conversion products, in addition to the desire to have high and stable output voltage, wider input voltage value, faster time response, and lower EMI, there is another very important indicator, that is, efficiency.

3.3. Sensor Energy Conversion. When comparator G discharges, a positive pulse appears at the output of the dead-time comparator, which is clocked by the pulse-constrained flip-flop, which simultaneously turns off transistors $Q1$ and $Q2$. If the output control terminal is connected to the reference voltage source, the modulated pulses are alternately output to the two output transistors, and the output frequency is equal to half of the pulse oscillator. In single-ended operation mode, when a higher drive current output is required, $Q1$ and $Q2$ can also be used in parallel. At this time, the output mode control pin must be connected to the ground to turn off the bistable flip-flop. In this state, the output pulse frequency of Figure 2 will be equal to the oscillator frequency.

The realization of the noninductive DC-DC converter is studied by replacing the actual inductive components with the general impedance converter, and the selection principle of each component in the circuit and the design scheme of the parameters are introduced in detail, within a certain dynamic range; the active analog inductance can replace the use of the coil inductance element, and the function of the inductance element can be well realized. The main reason for this phenomenon is that the transfer function of the feedback network has changed. In this paper, by connecting Cl in parallel at both ends of the ruler l and optimizing the design of the feedback resistor, the cross-over frequency hardly changes with the output voltage, which overcomes the effect of the output voltage change on the system response.

During the short-circuit test in Figure 3, the high-side SiC MOSFET in the parallel unit was kept on, and a 1 μs gate drive pulse was applied to the low-side SiC MOSFET. The HSF test switching waveforms of SiC MOSFETs $Q7$ and Q 8 in a parallel half-bridge cell with improved wiring are shown. For a buck converter, the ideal output voltage range is from the reference voltage to the supply voltage. Assuming that the internal reference voltage is 0.6 V, when the output voltage changes from 0.6 V to 0.8 V, the resistance ratio is changed from 1 to 4/3, the corresponding change in the cross-over frequency is 25%, and the change in stability is not serious at this time. In this way, even in the case of a heavy load, since the ESR value is small, the conduction loss relative to the element is small. At this time, Cl will play a positive role. The double-pulse experiment shows that compared with the traditional SiC parallel half-bridge unit, the transient current overshoot difference of the optimized parallel half-bridge unit with the parallel MOSFET at the lower arm is significantly reduced from 10.22% to 2.78%, and the switching loss difference is also obtained. The same degree of reduction and good transient current distribution also under fault short-circuit conditions. Steady-state experiments show that the optimized SiC parallel unit has a more uniform temperature distribution than the conventional parallel unit.

3.4. Device Current Balance Analysis. When the device current balance is put into a resistive load with a resistance value of 100 Ω, the waveforms of the output voltage and inductor current are shown below, when the resistive load is turned on in 0.3 s, the output voltage drops, the drop voltage is about 20 V, which is less than 5% of the output voltage, and it returns to the voltage command value of 700 V after a short time (about 0.2 s), which satisfies the stability. Therefore, D only affects spectral amplitudes below $fc1$ and even harmonic amplitudes, but the envelope of spectral amplitudes above $fc1$ is the same. In this section, the switching voltage waveform of the power device is approximately simplified into an ideal trapezoidal wave $(tr = tf)$ and a non-ideal trapezoidal wave $(tr \neq tf)$, and the influence of each time domain parameter of the switching waveform on its spectral characteristics is analyzed by the Fourier decomposition; and then, analyze the spectral characteristics of the switching voltage waveform of the SiC parallel half-bridge unit measured experimentally.

When the input resistance of the system in Figure 4 is 100 and the inductance is a resistive-inductive load of 300 mH, the waveforms of the output voltage and the

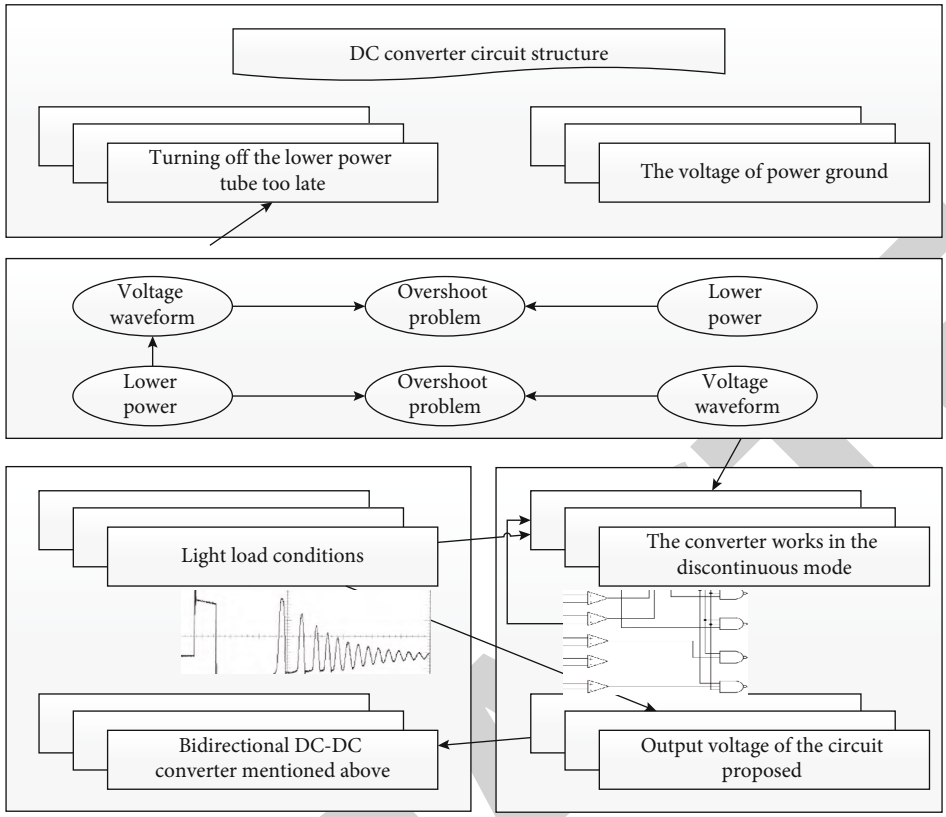

Figure 1: DC converter circuit structure.

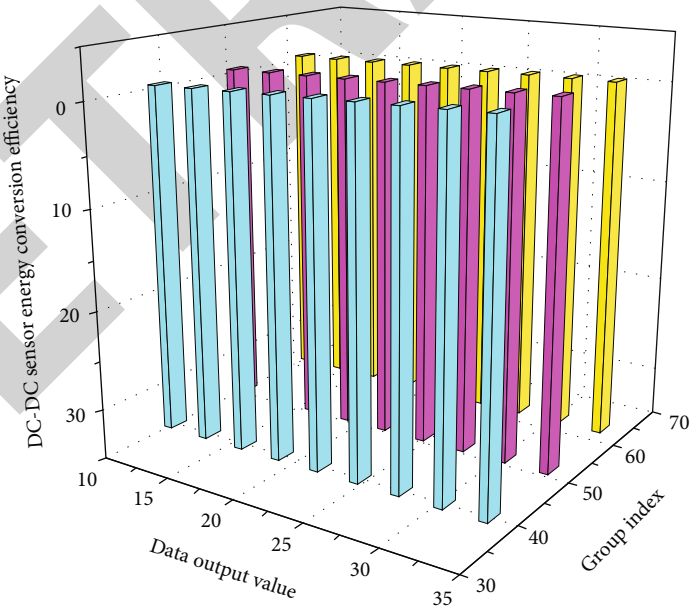

Figure 2: DC-DC sensor energy conversion efficiency output.

inductor current are shown in the figure. When the group inductive load is turned on for 0.3 s, the output voltage will drop to 15 V at this time. At this time, the output voltage can still recover to the command value of 700 V in a short period of time (about 0.5 s). For example, when selecting output filter capacitors, for this reason, some high-quality coefficient capacitors and multilayer ceramic capacitors are usually used, so that the output ripple equivalent input resistance can be ignored even at higher frequencies.

When the system is put into a constant power load, the waveforms of the output voltage and inductor current are shown. When the constant power load is put in under the

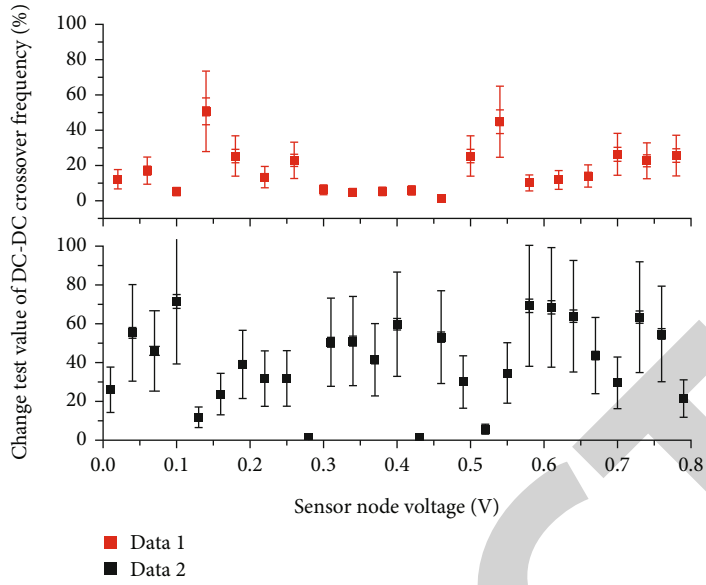

Figure 3: Variation test of the DC-DC sensor cross-over frequency.

load startup, the output voltage will also have a voltage drop. The drop value is 22 V, which is less than 5% of the output voltage, and it can still recover to the voltage command value. The steady-state recovery time is about 0.3 s. For the inductor current, after the constant power load is put on, the current value changes abruptly, and then it can return to a stable state. Note that the constant power load can still meet the system stability requirements under the voltage and current dual-mode control.

4. Model Application and Analysis of DC-DC Converter in Sensor and MEMS Device Integration and Packaging

4.1. DC-DC Converter Static Power Consumption. The specifications of the circuit should be consistent with the output voltage of 5 V output and define the current of light load as 0.1 A; the current of heavy load can reach 1 A. Therefore, the output power of this voltage converter can reach a maximum power output of 5 W, and in the tolerance of voltage regulation, it can withstand the fluctuation of the ripple voltage at 3%. When the input voltage drops from 15 V to 0 V, the time required is the drop time, and the conditions of the two converters under light load and heavy load are measured, respectively, as shown: among them, the traditional DC-DC conversion is displayed. The rise time of the device at light load and heavy load is divided into about 100 ms and 125 ms. For the fall time, at light load, the fall time is long due to the discharge of the energy storage element, and at heavy load because the electric energy is loaded by the load. The end absorbs quickly, so the fall time is short.

Therefore, the purpose of resonant soft switching technology is to reduce or even eliminate the loss caused by switching. The area becomes smaller or does not overlap, so the product of the voltage and current curves is reduced or zero, and of course, the purpose of reducing switching loss is achieved. According to the waveform of the upper tube current $i1$, in this process, the VT1 tube changes from the body IGBT conduction state in the IGBT mode to the diode conduction state; according to the lower tube current i2 waveform, it can be seen that the VT2 tube has been in the body IGBT cut-off state during this process. And the body diode is turned off. Figure 5 verifies the switching process of the RC-IGBT type bidirectional DC-DC converter from DC-DC mode to Boost mode.

Compared with the traditional DC-DC converter, it can be seen that the efficiency of the noninductive DC-DC converter is not very ideal, because the output current is provided by the general impedance converter circuit, which itself is a linear circuit composed of operational amplifiers. Although the efficiency does not meet expectations, the components that make up the noninductive DC-DC converter can be integrated, so its biggest feature is the opportunity to realize the integration of the entire voltage converter circuit, so as to achieve the purpose of miniaturization.

4.2. Design of Shutdown Circuit of Microcomputer System. The test results of the conducted interference when the computer system is turned off are shown. In the low-frequency band (less than 6.5 MHz) and the 7.5 MHz-10 MHz frequency band, the front-stage AC/DC converter is the main source of the common-mode interference in the DC-DC system; due to the output power, the high-frequency transmission line effect of the inductor and the series resonance of the output negative lead inductance cause the common-mode interference of the poststage DC-DC converter to have a maximum value at 7.1 MHz. According to the wire selection table, you can use 1 strand of AWG10 enameled wire or use 2 strands of AWG13 enameled wire to be wound in parallel. Common-mode inductors are generally wound with a single-strand wire, which is not only low-cost but also helps to attenuate high-frequency noise due to the AC copper loss caused by the high-frequency skin effect.

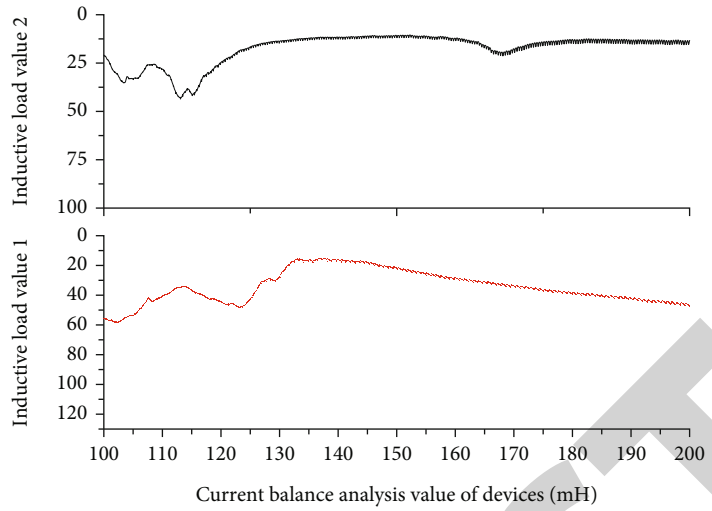

Figure 4: Current balance analysis of resistive and inductive load devices.

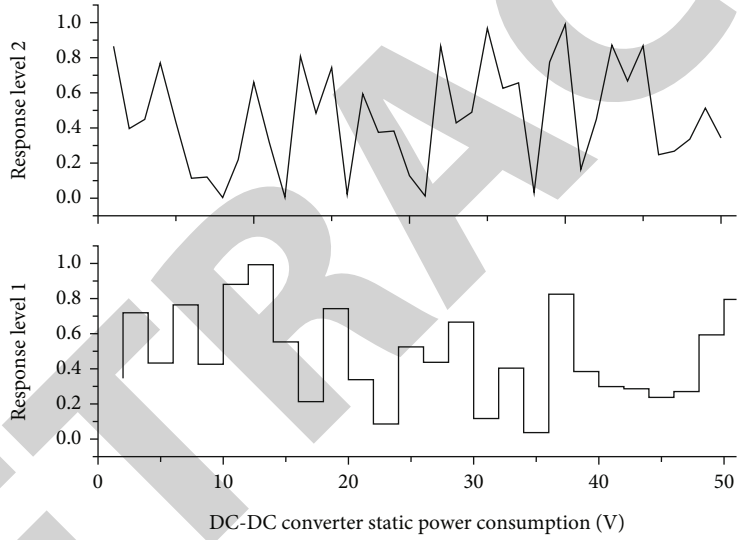

Figure 5: DC-DC converter static power dissipation response.

In order to increase the number of winding turns and reduce the distributed capacitance of the winding, use the same winding method as the power inductor and wind 2 strands of AWG13 enameled wire in parallel. The power inductor uses an equivalent single-layer winding method, which can reduce its parasitic equivalent parallel capacitance, significantly improve its high-frequency impedance characteristics (+19 dB), and suppress its series resonance effect with the parasitic inductance of the Boost input negative lead, thereby inhibiting the common-mode-conducted interference in a specific frequency band.

The working mode identification link is mainly based on the inductor current direction information obtained through the double hysteresis link, combined with the conventional PWM signal. Figure 6 obtains the current working status of the upper and lower tubes, so as to design the required drive control content. The working mode of the RC-IGBT tube is divided into two modes: the IGBT mode and diode mode. When analyzing the various states of the RC-IGBT power tube, the influence of the dynamic process needs to be considered. In the IGBT mode, the RC-IGBT power tube needs to add a period of IGBT dead zone stage and wait for the tube desaturation stage on the basis of the original several states. These include the following: doubling the duty cycle for a given input and output step-down ratio; the maximum drain-source voltage of most power switches is only VIN/2; and each time the converter is powered on, the internal precharge circuit will charge the energy transfer capacitors CT1 and CT3 first, until the voltage on both sides of the capacitor reaches half of the input voltage V, and then the power switch is connected. The analysis method of the DC PWM converter is the proposed simplified three-terminal PWM switch model, which only consists of an active switch SW and a passive switch VD.

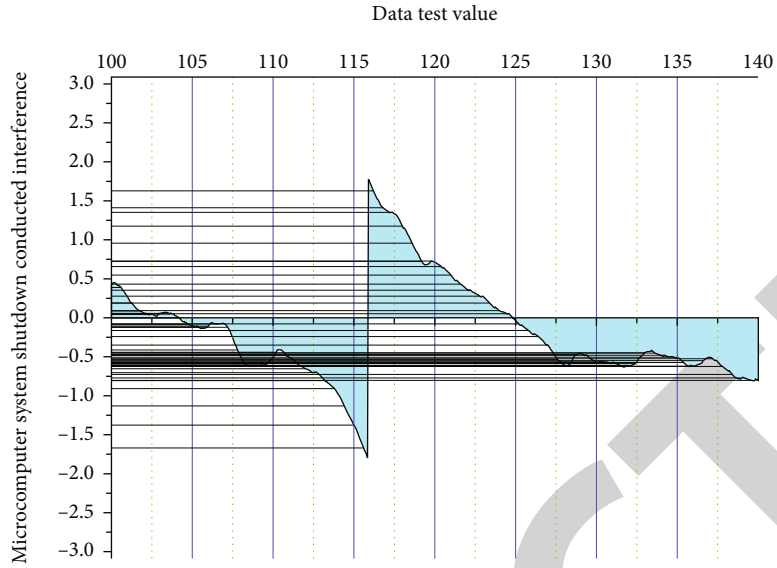

Figure 6: Microcomputer system shutdown conducted interference test.

Table 1: Microcomputer system integration algorithm.

Microcomputer system	Integration algorithm codes
For j in range (size pop)	$R(x)C(x)$
Result = np.zeros(maxgen)	The premise of not adding $dx(k)$
Result[i] = gbestfitness	Additional suppressing devices
W = getweight()	Conducted interference characteristics
Lr = getlearningrate()	DC-DC system studied $dy(k)$
Maxgen = getmaxgen()	Illustrate the influence
Sizepop = getsizepop()	The shielded cable $R(x) - C(x)$
Rangepop = getrangepop()	On the AC grid side
Pop, v, fitness = initpopvfit(sizepop)	In order to $1 - f(x)C(x)$
Gbestpop, gbestfitness, pbestpop,	On the conducted interference
Pbestfitness = getinitbest(fitness, pop)	The nonisolated $i(res)$
V[v < rangespeed[0]] = rangespeed[0]	High-voltage battery side $i(sense)$
V[v > rangespeed [1]] = rangespeed [1]	Characteristics of the vehicle

In order to illustrate the influence of the shielded cable on the AC grid side of the nonisolated DC-DC system studied in this paper on the conducted interference characteristics of the vehicle high-voltage battery side, Table 1 tests the DC-DC system without using the input shielded cable (equivalent to isolation). The control circuit includes an output sampling network, an error amplifier, a compensator, a pulse-width modulator, and a power switch. Under the premise of not adding additional suppressing devices, the high-frequency impedance characteristics of the power inductor can be improved by changing the winding method of the power inductor, which can significantly suppress the grid side-conducted interference of the multiplexer converter in the DC-DC mode in the frequency range of 1 MHz to 30 MHz. However, the DC-DC grid side-conducted interference as a whole does not meet the Class B limit in CISPR32, so a filter needs to be added to further suppress the DC-DC grid side-conducted interference.

4.3. Device Integration and Package Simulation. This section mainly analyzes the influence of different desaturation delays on the output voltage through simulation and compares the output voltage waveforms after adding carrier asymmetric modulation and before adding desaturation pulses to verify its suppressing effect on dead zone. In general, the switching frequency of the RC-IGBT is lower than that of the conventional IGBT, so the switching frequency is set to 2 kHz, the input voltage V of the step-down ratio chip ranges from 10 to 12 V, and the gate drive high voltage when the GaN power switch is fully turned on. The level is

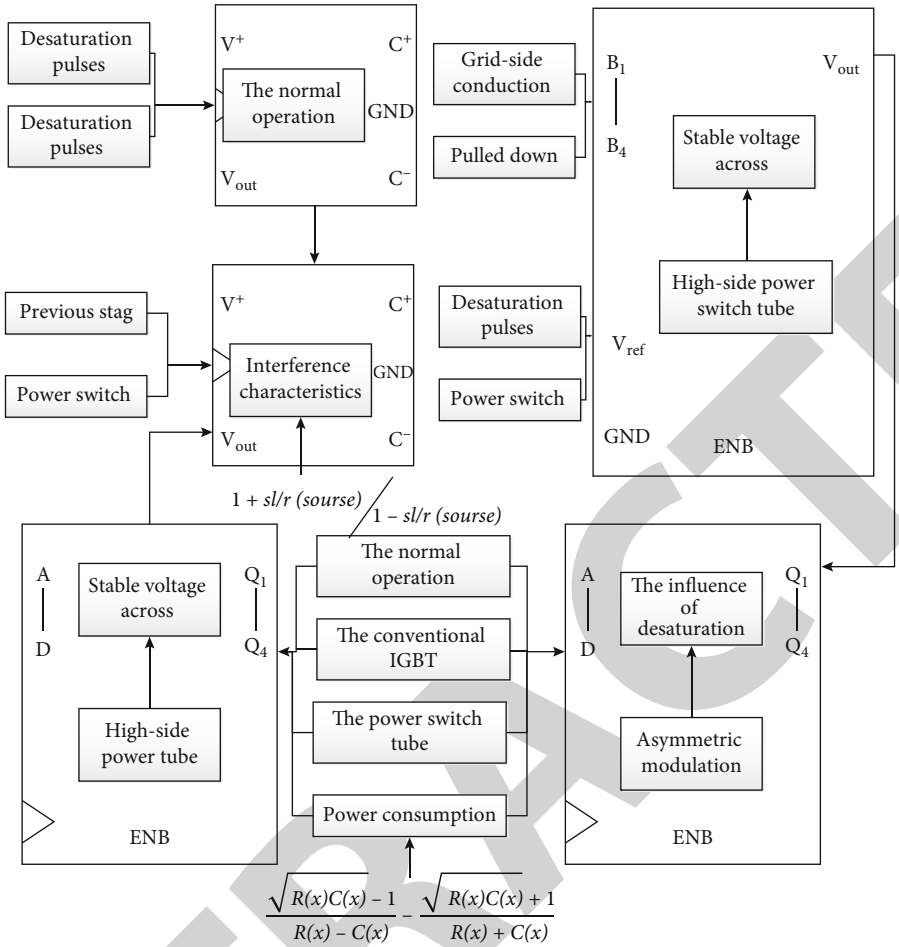

Figure 7: DC-DC device integration topology.

Table 2: DC-DC grid side conduction properties.

DC-DC mode	Conduction mode	Frequency/MHz	Grid side error	Grid side rate
Converter *a*	Negative lead	5.48	1.83	0.61
Converter *b*	Conducted mode	2.91	0.97	0.32
Converter *c*	Parasitic inductance	7.69	2.56	0.85
Converter *d*	Key components	3.34	1.11	0.37
Converter *e*	Full-load current	2.35	0.78	0.26
Converter *f*	Current rating	14.15	1.83	0.61

4~6 V, and the range includes $VrN/2$. When driving the upper power tubes S1A, S2A, S3A, and S4A of the high-voltage side, a floating voltage source is required to ensure the normal operation of the driving circuit.

Figure 7 uses a bootstrap floating power supply that floats relative to the Vs voltage. Its level generation method is similar to that of a charge pump: whenever the duty cycle signal drives the high-side power switch to turn off, the Vs voltage is pulled down. After adding asymmetric carrier modulation, the voltage ripple is significantly reduced, and the desaturation process is added compared to when no desaturation pulse is added, so that the loss of the RC-IGBT body diode is lower when it is turned off, and the power consumption is reduced.

4.4. Example Application and Analysis. From the theoretical analysis of the conducted interference characteristics of the DC-DC grid side, it can be known that the conducted interference characteristics of the AC grid side mainly depend on the AC/DC converter of the previous stage, and the conducted interference characteristics of the AC/DC converter of the previous stage largely depend on the input power inductance. By improving the high-frequency impedance characteristics of the input power inductor, it can suppress

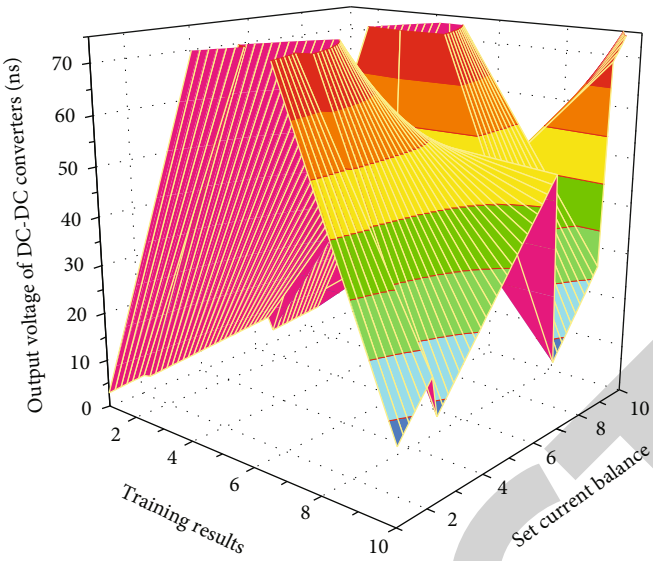

Figure 8: Balanced distribution of output voltage and current of the DC-DC converter.

the high-frequency- (1 MHz-30 MHz) conducted interference on the DC-DC grid side and reduce the high-frequency attenuation requirement for the grid side filter. By adding a small package X-capacitor at the DC-DC output to reduce the parasitic inductance of the negative lead, this scheme can significantly suppress the conducted interference spike of the poststage DC-DC converter in the 7.15 MHz frequency band. The commonly used methods are voltage-type and current-type control. Here, we will focus on the voltage-based control method. The basic principle of the voltage-type control method is to compare the output signal of the error amplifier with a fixed frequency triangular wave to generate a PWM signal for control.

The total volume of the peripheral key components in Table 2 is calculated by multiplying the height of the highest component in the converter by the external power switch tube (if any), output capacitor, inductor, external current sampler (if any), and series connection. If the output control terminal is connected to the reference voltage source, the modulation pulse is output to the two output transistors alternately, and the output frequency is equal to half of the pulse oscillator.

The resistors and capacitors used in the current sampler in this converter are all 0201 packages, and the total surface area of the four components is 0.72 mm. Since a four-phase design is used to share the current, and the proposed current balancing strategy reduces the current rating requirement of each inductor, each inductor can use the smallest package. The designed converter still has the lowest height and the smallest overall volume of critical peripheral components, thus achieving extremely high current density. In addition, due to the miniaturization of the inductor, the height of the converter is reduced from the traditional 7.5-3 mm to 0.9 mm, and the designed converter can be applied to extremely flat occasions, which is beneficial to the thinning of portable products.

When the current balancing function is turned off, the mismatch of the input offset in Figure 8 results in a 30 ns error in the conduction time of the upper tube, while the rated value should be 80 ns, resulting in an imbalance of 1.54A in the average inductor current between phases. The inductors carry 75% more current than the other phases. As a result, when the current balancing function is turned on, the inductor currents of all four phases are almost the same, and the phases are evenly interleaved by 900. The transient responses of the four-phase DC-DC converter under positive and negative load step changes are shown, respectively, and the load change range is 4 A-8 A, the load change rate is 4 A/ps, the same comparator input offset is still retained at this time, and it can be seen that the four-phase currents are still followed and equal. This proves that the proposed current balancing scheme can solve the current imbalance problem well in both steady state and transient state.

5. Conclusion

Starting from the output voltage ripple components of the multiphase DC-DC converter, an integrated package model of the multiphase DC-DC converter is constructed in this paper. According to the requirements of simple implementation and fast load transient response, the model proposes and designs an adaptive on-time control logic based on ripple feedback. By analyzing the reverse inductor current detection mechanism, a low-cost self-calibrating zero-current switch is proposed circuit breaker; by analyzing the abnormal driving signal caused by the transmission delay, the high-reliability power switch tube driving logic is perfected. This is suitable where the transformer has a feedback winding and a capture diode is used, i.e., the output transformer has a feedback winding and the diode provides the feedback voltage. The primary side controller adopts the high-voltage power tube integration and high-voltage power supply scheme of the aforementioned constant current controller, so that the primary side controller has a simple peripheral circuit, while the secondary side controller

integrates the synchronous rectifier controller to improve the flyback conversion efficiency of the device. The 18BCD process tape-out test and the results are compared to verify the effects of various characteristics of the two-phase DC-DC converter.

Data Availability

The data used to support the findings of this study are available from the corresponding author upon request.

Conflicts of Interest

The authors declare that they have no known competing financial interests or personal relationships that could have appeared to influence the work reported in this paper.

Acknowledgments

This work was supported by the School of Science and Technology, University of Sanya.

References

[1] X. Guo, Q. Xun, Z. Li, and S. du, "Silicon carbide converters and MEMS devices for high-temperature power electronics: a critical review," *Micromachines*, vol. 10, no. 6, p. 406, 2019.

[2] D. Dinulovic, M. Shousha, M. Haug et al., "Microfabricated magnetics on silicon for point of load high-frequency DC–DC converter applications," *IEEE Transactions on Industry Applications*, vol. 55, no. 5, pp. 5068–5077, 2019.

[3] M. Touhami, G. Despesse, T. Hilt et al., "Piezoelectric materials for the dc-dc converters based on piezoelectric resonators," in *Workshop on Control and Modelling of Power Electronics (COMPEL). IEEE*, pp. 5–8, Cartagena, Colombia, 2021.

[4] H. T. Le, R. I. Haque, Z. Ouyang et al., "MEMS inductor fabrication and emerging applications in power electronics and neurotechnologies," *Microsystems & Nanoengineering*, vol. 7, no. 1, pp. 21-22, 2021.

[5] M. Parvez, A. T. Pereira, N. Ertugrul, N. H. E. Weste, D. Abbott, and S. F. al-Sarawi, "Wide bandgap DC–DC converter topologies for power applications," *Proceedings of the IEEE*, vol. 109, no. 7, pp. 1253–1275, 2021.

[6] H. Li, K. Zhu, K. Lei, T. Xu, and H. Wu, "Integrated MEMS toroidal transformer with Ni-Zn ferrite core for power supply on chip," *IEEE Transactions on Power Electronics*, vol. 37, no. 9, pp. 10075–10080, 2022.

[7] A. Barbieri, M. Zamprogno, L. Molinari et al., "Fully integrated system-in-package device for drive, sense, and control of MEMS μmirrors for Raster scan projection," *MOEMS and Miniaturized Systems XXI. SPIE*, vol. 12013, pp. 67–78, 2022.

[8] C. Sano, M. Ataka, G. Hashiguchi, and H. Toshiyoshi, "An electret-augmented low-voltage MEMS electrostatic out-of-plane actuator for acoustic transducer applications," *Micromachines*, vol. 11, no. 3, p. 267, 2020.

[9] N. T. Tasneem, D. K. Biswas, P. R. Adhikari et al., "A self-powered wireless motion sensor based on a high-surface area reverse electrowetting-on-dielectric energy harvester," *Scientific Reports*, vol. 12, no. 1, pp. 12–15, 2022.

[10] M. Duque, E. Leon-Salguero, J. Sacristán, J. Esteve, and G. Murillo, "Optimization of a piezoelectric energy harvester and design of a charge pump converter for CMOS-MEMS monolithic integration," *Sensors*, vol. 19, no. 8, p. 1895, 2019.

[11] S. Seok, C. Wang, E. Lefeuvre, and J. Park, "Autonomous energy harvester based on textile-based enzymatic biofuel cell for on-demand usage," *Sensors*, vol. 20, no. 17, article 5009, 2020.

[12] M. Paesler, T. Lisec, and H. Kapels, "Novel integrated BEOL compatible inductances for power converter applications," in *Applied Power Electronics Conference and Exposition (APEC). IEEE*, pp. 2647–2652, New Orleans, LA, USA, 2020.

[13] R. Rady, H. Dogan, M. Aktan, S. A. Mohammed, and M. T. Ozgun, "An ultra low power integrated radio TX link supplied from a switched capacitor DC–DC converter in 65-nm CMOS achieving 2 mbps," *IEEE Transactions on Circuits and Systems II: Express Briefs*, vol. 67, no. 10, pp. 1899–1903, 2019.

[14] J. D. Boles, J. J. Piel, N. Elaine, J. E. Bonavia, J. H. Lang, and D. J. Perreault, "Piezoelectric-based power conversion: recent progress, opportunities, and challenges," in *Custom Integrated Circuits Conference (CICC). IEEE*, pp. 5–8, Newport Beach, CA, USA, 2022.

[15] A. Martins, M. Pinheiro, A. F. Ferreira et al., "Heterogeneous integration challenges within wafer level fan-out SiP for wearables and IoT," in *Electronic Components and Technology Conference (ECTC). IEEE*, pp. 1485–1492, San Diego, CA, USA, 2018.

[16] C. Shetty, "A detailed study of Qdc of 3D micro air-core inductors for integrated power supplies: power supply in package (PSiP) and power supply on chip (PSoC)," *Power Electronic Devices and Components*, vol. 2, article 100006, 2022.

[17] L. Liu, Y. Ou, J. Ma, Y. Xie, and Y. Yu, "An inductorless P-SSHC piezoelectric energy harvesting integrated system with high flipping efficiency," *Microelectronics Journal*, vol. 125, article 105479, 2022.

[18] S. Ji and X. Liao, "Researches on MEMS thermoelectric-photoelectric integrated energy harvester with metal heat sink," *Microelectronics Journal*, vol. 96, article 104702, 2020.

[19] J. T. Stauth, "Pathways to mm-scale DC-DC converters: trends, opportunities, and limitations," in *Custom Integrated Circuits Conference (CICC). IEEE*, pp. 4–8, San Diego, CA, USA, 2018.

[20] D. Jordan, G. Wei, L. Ye et al., "High q-factor pcb embedded flip-chip inductors with multilayer cztb magnetic sheet for power supply in package (pwrsip)," *IEEE Journal of Emerging and Selected Topics in Power Electronics*, vol. 9, no. 1, pp. 102–110, 2021.

[21] M. Duque, E. Leon-Salguero, J. Sacristán, J. Esteve, and G. Murillo, "Towards the monolithic integration of converter circuitry and piezoelectric MEMS energy harvesters," in *Multidisciplinary Digital Publishing Institute Proceedings*, vol. 2, Graz, Austria, 2018no. 13, Article ID 1512.

[22] S. Nabavi and L. Zhang, "T-shaped piezoelectric structure for high-performance MEMS vibration energy harvesting," *Journal of Microelectromechanical Systems*, vol. 28, no. 6, pp. 1100–1112, 2019.

[23] M. Ali, M. Nabavi, A. Hassan, M. Honarparvar, Y. Savaria, and M. Sawan, "A versatile SoC/SiP sensor interface for industrial applications: design considerations," in *Microelectronics (ICM). IEEE*, pp. 40–43, Cairo, Egypt, 2019.